



Title	Improving the tensile properties of additively manufactured $\beta$ -containing tial alloys via microstructure control focusing on cellular precipitation reaction
Author(s)	Cho, Ken; Odo, Hirotaka; Okamoto, Keisuke et al.
Citation	Crystals. 2021, 11(7), p. 809
Version Type	VoR
URL	<a href="https://hdl.handle.net/11094/89778">https://hdl.handle.net/11094/89778</a>
rights	This article is licensed under a Creative Commons Attribution 4.0 International License.
Note	


*The University of Osaka Institutional Knowledge Archive : OUKA*

<https://ir.library.osaka-u.ac.jp/>

The University of Osaka

## Article

# Improving the Tensile Properties of Additively Manufactured $\beta$ -Containing TiAl Alloys via Microstructure Control Focusing on Cellular Precipitation Reaction

Ken Cho <sup>1,2</sup>, Hirotaka Odo <sup>1</sup>, Keisuke Okamoto <sup>1</sup>, Hiroyuki Y. Yasuda <sup>1,2,\*</sup>, Hirotoyo Nakashima <sup>3</sup>, Masao Takeyama <sup>3</sup> and Takayoshi Nakano <sup>1,2</sup> 

<sup>1</sup> Division of Materials and Manufacturing Science, Graduate School of Engineering, Osaka University, 2-1 Yamadaoka, Suita, Osaka 565-0871, Japan; k\_cho@mat.eng.osaka-u.ac.jp (K.C.); hirotaka.odo@mat.eng.osaka-u.ac.jp (H.O.); keisuke.okamoto@mat.eng.osaka-u.ac.jp (K.O.); nakano@mat.eng.osaka-u.ac.jp (T.N.)

<sup>2</sup> Anisotropic Design & Additive Manufacturing Research Center, Graduate School of Engineering, Osaka University, 2-1 Yamadaoka, Suita, Osaka 565-0871, Japan

<sup>3</sup> Department of Materials Science and Engineering, School of Materials and Chemical Technology, Tokyo Institute of Technology, 2-12-1 Ookayama, Meguro-ku, Tokyo 152-8552, Japan; nakashima.h.aa@m.titech.ac.jp (H.N.); takeyama@mtl.titech.ac.jp (M.T.)

\* Correspondence: hyasuda@mat.eng.osaka-u.ac.jp



**Citation:** Cho, K.; Odo, H.; Okamoto, K.; Yasuda, H.Y.; Nakashima, H.; Takeyama, M.; Nakano, T. Improving the Tensile Properties of Additively Manufactured  $\beta$ -Containing TiAl Alloys via Microstructure Control Focusing on Cellular Precipitation Reaction. *Crystals* **2021**, *11*, 809.

<https://doi.org/10.3390/cryst11070809>

Academic Editor: Umberto Prisco

Received: 18 June 2021

Accepted: 9 July 2021

Published: 12 July 2021

**Publisher's Note:** MDPI stays neutral with regard to jurisdictional claims in published maps and institutional affiliations.



**Copyright:** © 2021 by the authors. Licensee MDPI, Basel, Switzerland. This article is an open access article distributed under the terms and conditions of the Creative Commons Attribution (CC BY) license (<https://creativecommons.org/licenses/by/4.0/>).

**Abstract:** The effect of a two-step heat treatment on the microstructure and high-temperature tensile properties of  $\beta$ -containing Ti-44Al-4Cr (at%) alloys fabricated by electron beam powder bed fusion were examined by focusing on the morphology of  $\alpha_2/\gamma$  lamellar grains and  $\beta/\gamma$  cells precipitated at the lamellar grain boundaries by a cellular precipitation reaction. The alloys subjected to the first heat treatment step at 1573 K in the  $\alpha + \beta$  two-phase region exhibit a non-equilibrium microstructure consisting of the  $\alpha_2/\gamma$  lamellar grains with a fine lamellar spacing and a  $\beta/\gamma$  duplex structure located at the grain boundaries. In the second step of heat treatment, i.e., aging at 1273 K in the  $\beta + \gamma$  two-phase region, the  $\beta/\gamma$  cells are discontinuously precipitated from the lamellar grain boundaries due to excess Cr supersaturation in the lamellae. The volume fraction of the cells and lamellar spacing increase with increasing aging time and affect the tensile properties of the alloys. The aged alloys exhibit higher strength and comparable elongation at 1023 K when compared to the as-built alloys. The strength of these alloys is strongly dependent on the volume fraction and lamellar spacing of the  $\alpha_2/\gamma$  lamellae. In addition, the morphology of the  $\beta/\gamma$  cells is also an important factor controlling the fracture mode and ductility of these alloys.

**Keywords:** additive manufacturing; electron beam powder bed fusion; titanium aluminide; microstructure; cellular precipitation reaction; tensile properties

## 1. Introduction

Titanium aluminide (TiAl) alloys have attracted significant interest for high-temperature applications such as aircraft and automotive engines because of their lightweight characteristics, excellent strength at high temperatures, and good oxidation resistance [1,2]. In fact, Ti-48Al-2Cr-2Nb (at%, hereafter referred to as 48-2-2) alloys which are known as second-generation TiAl alloys can drastically improve the efficiency of aero-jet engines by reducing their weight as they can be used to replace nickel-based superalloys in low-pressure turbine (LPT) blades [3,4]. In general, TiAl alloys consist of Ti<sub>3</sub>Al ( $\alpha_2$ ) phase with the D0<sub>19</sub> structure and TiAl ( $\gamma$ ) phase with the L1<sub>0</sub> structure [1–4]. A unique lamellar structure composed of the  $\alpha_2$  and  $\gamma$  phases is formed, satisfying the Blackburn orientation relationship as follows.

$$(111)\gamma // (0001)\alpha_2, \left[ \begin{smallmatrix} \bar{1} & 1 & 0 \end{smallmatrix} \right] \gamma // \left[ \begin{smallmatrix} 1 & 1 & 2 \end{smallmatrix} \right] \alpha_2 \quad (1)$$

The lamellar structure is favorable for high-temperature strength and good fracture toughness at room temperature. In recent years, a new concept for controlling the microstructure of the TiAl alloys, which is focused on an ordered  $\beta$  phase with the B2 structure, has been proposed by Takeyama et al. [5]. The new type of TiAl alloys, such as Ti-Al-Nb-Mo-B (TNM) alloys, developed based on this new concept are categorized as  $\beta$ -containing TiAl alloys and have been widely studied in terms of their microstructure, mechanical properties, and oxidation behavior [6,7]. These new-generation alloys are expected not only to improve the efficiency of the jet engines but also to expand the application scope of the TiAl alloys as they exhibit mechanical properties much superior to those of conventional alloys (e.g., 48-2-2 alloys) at high temperatures [8–11].

However, there are significant concerns about contamination and oxidation of the surface when the TiAl parts are manufactured by the existing processes such as precision investment casting [12–14]. Therefore, it is necessary to develop a new manufacturing process for the TiAl alloys to overcome these problems.

Additive manufacturing (AM) processes can fabricate near-net-shaped parts directly from raw metal powders based on three-dimensional computer-aided design (3D-CAD) data. These processes have attracted much attention as efficient fabrication processes for metal products with complex shapes in the aerospace and biomedical industries and elsewhere [15–18]. In particular, an electron beam powder bed fusion (EB-PBF) of which the heat source is a focused electron beam is considered to be a suitable fabrication process for highly reactive materials because the process is done in vacuum, which can prevent contamination and oxidation of the part surfaces [19–21]. More importantly, the microstructure and the mechanical properties of the alloy parts fabricated by AM can be controlled by optimizing process parameters and scan strategies based on the shape and thermal gradient of the melt pool and solidification rate [22–28]. In particular, the mechanical anisotropy originating from microstructural anisotropy is one of the important features for the alloy fabricated by AM process [29–32]. In our previous studies, we found that it is possible to obtain TiAl alloys with unique microstructures by repeated and rapid fusion and solidification of metal powders, which is a unique phenomenon during the EB-PBF process [33,34]. In the case of the 48-2-2 alloys manufactured by EB-PBF, the layered microstructure composed of an equiaxed  $\gamma$  grain region (referred to as  $\gamma$  band) and a duplex-like region formed by repeated thermal effects from the melt pool can be obtained at specific process conditions. The localized deformation in the  $\gamma$  band resulted in a large elongation at room temperature (>2.5%) and excellent fatigue properties at high temperatures [33,35–37]. Moreover, the  $\beta$ -containing Ti-44Al-4Cr (at%, hereafter referred to as 44-4) alloys fabricated by EB-PBF reveal very fine structures containing fine  $\alpha_2/\gamma$  lamellar grains with a lamellar spacing of approximately 30 nm. The fine lamellar grains which are referred to as ultrafine lamellar grains are formed through a massive  $\alpha$  phase transformation, resulting from the rapid cooling of the melt pool and its vicinity [34]. We also found that the alloys containing the ultrafine lamellar grains exhibit high strength at room temperature and high temperatures [34]. These studies suggest that EB-PBF can fabricate the TiAl parts with improved mechanical properties while overcoming the concerns associated with conventional manufacturing processes.

To increase the reliability of the TiAl parts fabricated by EB-PBF, it is necessary to subject the hot isostatic pressing (HIP) treatment to eliminate any small defects or fine pores generated by a lack of fusion or the atomization gas trapped in the raw powder, respectively. The HIP temperature for the TiAl alloys is in the range of 1573–1273 K and this treatment has a significant effect on the microstructure [38,39]. This, in turn, changes the mechanical properties of the alloys. However, HIP or heat treatment conditions to improve mechanical properties of the  $\beta$ -containing TiAl alloys fabricated by EB-PBF have not been investigated yet.

Therefore, in the present study, we designed a two-step heat treatment process for improving the high-temperature tensile properties of the  $\beta$ -containing TiAl alloy parts fabricated by EB-PBF in anticipation of application to the HIP process. The first heat treat-

ment is done at 1573 K in the  $\alpha + \beta$  two-phase region, followed by air cooling, to introduce the fine  $\alpha_2/\gamma$  lamellar grains which are expected to increase alloy strength [34,40,41]. The second heat treatment at 1273 K in the  $\beta + \gamma$  two-phase region aims at precipitating a  $\beta/\gamma$  cell structure from the lamellar grain boundary by the cellular precipitation reaction (discontinuous precipitation reaction), which has been reported to improve the fracture toughness and the crack-propagation resistance during cyclic deformation [42]. The microstructure of the resultant heat-treated alloys was quantitatively analyzed with respect to the heat treatment time. In addition, the influence of the microstructure on the tensile properties and fracture mode of the  $\beta$ -containing alloys at high temperatures was examined via tensile tests at 1023 K and fracture-surface analysis.

## 2. Materials and Methods

### 2.1. Sample Fabrication by EB-PBF

The  $\beta$ -containing 44-4 alloy was used in this study [38]. Raw alloy powder with a mean diameter of approximately 70  $\mu\text{m}$  was prepared by Ar gas atomization at Osaka Yakin Kogyo Co., Ltd., Osaka, Japan, from master ingots provided by Kobe Steel, Ltd., Kobe, Japan.

We used an Arcam Q10 EB-PBF system to fabricate rectangular rods with dimensions of 10  $\times$  10  $\times$  30 mm from the raw alloy powder. The accelerating voltage, the pre-heating temperature, and the layer thickness for each powder layer were set at 60 kV, 1333 K, and 90  $\mu\text{m}$ , respectively. It should be noted that the building direction was parallel to the longitudinal direction of the rods. Figure 1a shows the as-built 44-4 alloy rod fabricated by EB-PBF. Noted that the bottom part of the rod is a support for precise fabrication. The dimensional error of the as-built rods is smaller than 0.3 mm, indicating that the process conditions used in the present study are suitable for fabrication of the 44-4 alloy rods with high structural integrity. The chemical composition of the as-built rods was analyzed by an inductively coupled plasma optical emission spectroscopy (Al, Cr) and an inert gas fusion method (O) (Table 1). It should be noted that the O content of the alloy rods, which has significant influence on the microstructure and mechanical properties, is comparable to that of the raw powder (0.15 at%), indicating limited oxidation during the fabrication process. It is noted that the porosity of the as-built rods is less than 0.3%. Such a small amount of pore has no significant influence on tensile properties [34]. The details of the fabrication process and characteristics of the as-built rods, including their structural integrity (internal defect and porosity), can be found in our previous report [34].

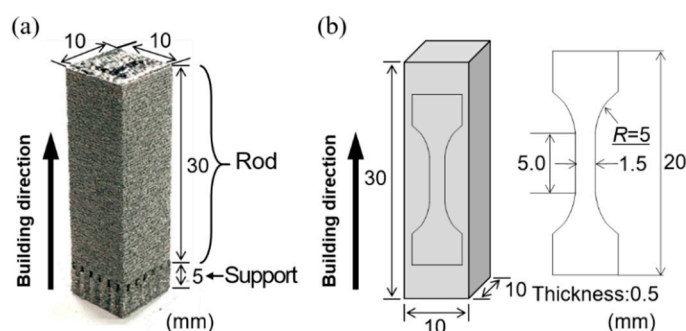


**Figure 1.** An as-built 44-4 alloy rod fabricated by EBM (a) and schematic drawings of the rod and the specimen configuration for tensile tests (b).

**Table 1.** Chemical composition of the 44-4 alloy rods fabricated by EBM.

	Ti	Al	Cr	O
Nominal composition	Bal.	44	4	0
Actual composition	Bal.	43.9	4.0	0.18

## 2.2. Heat Treatment

To obtain the  $\alpha_2/\gamma$  lamellar structure surrounded by the  $\beta/\gamma$  cells at the lamellar boundaries, the as-built rods were subjected to a two-step heat treatment process at different temperatures derived from the phase diagram [38]. The first heat treatment step was conducted at 1573 K in the  $\beta + \alpha$  two-phase region, for 2 or 4 h in an Ar atmosphere, followed by air cooling as a solution treatment (ST). Hereafter, the alloys solutionized for 2 and 4 h are referred to as 2ST and 4ST, respectively. The solutionized rods were then subjected to aging (AG) at 1273 K in the  $\beta + \gamma$  two-phase region, for 0.1, 0.5, 1, or 24 h in an Ar atmosphere followed by air cooling; these aged alloys are referred to as 0.1AG, 0.5AG, 1AG, and 24AG, respectively.

## 2.3. Material Characterization

The microstructure of the alloy rods was observed using a X-ray diffractometer (XRD), a field-emission scanning electron microscope (FE-SEM) equipped with a back-scattered electron (BSE) detector, and a transmission electron microscope (TEM) operated at 15 kV and 300 kV, respectively. XRD analyses were performed using a Cu target at an acceleration voltage of 40 kV and a current of 30 mA. The plates required for the microstructure observations were cut parallel to the longitudinal direction (building direction) of the rectangular rods by electro-discharge machining and mechanically polished with SiC waterproof emery papers of up to #2000 grit and subsequently electrically polished in an  $\text{HClO}_4$ :butanol:methanol (6:35:59 vol.%) solution. The morphology of the  $\alpha_2/\gamma$  lamellar and the  $\beta/\gamma$  cell structures was quantitatively analyzed from the SEM-BSE images using the image analysis software, ImageJ.

The high-temperature tensile properties of the as-built and annealed alloys were examined using an Instron-type testing machine at 1023 K in a vacuum with an initial strain rate of  $1.7 \times 10^{-4} \text{ s}^{-1}$ . Tensile specimens with gauge dimensions of  $5.0 \times 1.5 \times 1.0 \text{ mm}$  were cut by electro-discharge machining from the alloy bars (Figure 1b). The surfaces of the specimens were polished using SiC waterproof emery papers and a colloidal  $\text{SiO}_2$  suspension. The fracture surfaces and side view of fracture parts of the tensile-deformed specimens were carefully observed using an FE-SEM. The hardness of each constituent structure was measured by nanoindentation tests with a maximum load of 59 mN at room temperature.

## 3. Results and Discussion

### 3.1. Effect of the Two-Step Heat-Treatment Process on the Microstructure

Figure 2a shows the typical XRD profiles of the rods before and after solution treatment for 4 h. The as-built and solutionized rods consist of the  $\alpha_2$ ,  $\gamma$ , and  $\beta$  phases. Figure 2b–e exhibits the microstructure of the as-built and 2ST and 4ST rods, in which the  $\alpha_2$ ,  $\gamma$ , and  $\beta$  phases exhibit gray, black, and white contrasts, respectively. The as-built rods consist of a fine  $\alpha_2/\beta/\gamma$  mixed structure, the ultrafine  $\alpha_2/\gamma$  lamellar grains, and the  $\beta/\gamma$  cells (Figure 2b,c). It should be noted that the microstructure of the as-built rods is much finer than that of cast and forged alloys (grain size: 100–800  $\mu\text{m}$ ) [43,44], owing to rapid solidification and cooling during EB-PBF. The formation mechanism of the fine as-built microstructure was investigated in a previous study [34]. As shown in Figure 2d,e, the microstructure changes completely upon solution treatment at 1573 K. The 2ST and 4ST contain the equiaxed  $\alpha_2/\gamma$  lamellar grains with a  $\beta/\gamma$  duplex structure at the grain boundaries. It is noted that the solutionized rods have uniform and isotropic microstructure. The  $\alpha_2/\gamma$  lamellar grains and the  $\beta/\gamma$  duplex structure are formed from the single  $\alpha$  grains and the  $\beta$  phases by the precipitation of the  $\gamma$  phase during the air cooling, respectively. The mean diameters of the  $\alpha_2/\gamma$  lamellar grains ( $D_L$ ) in 2ST and 4ST are approximately 37 and 36  $\mu\text{m}$ , respectively. This indicates that  $D_L$  in 2ST and 4ST is higher than that of the grains in the as-built samples but lower than that of alloys fabricated by conventional processes [45]. This difference is attributed to the fine initial microstructure of the as-built rods (Figure 2b,c). In addition, the  $\beta$  phase precipitated at the grain boundaries suppresses



the growth of the  $\alpha$  grains by grain-boundary pinning. Consequently,  $D_L$  is insensitive to heat treatment time, as shown in Figure 2d,e).

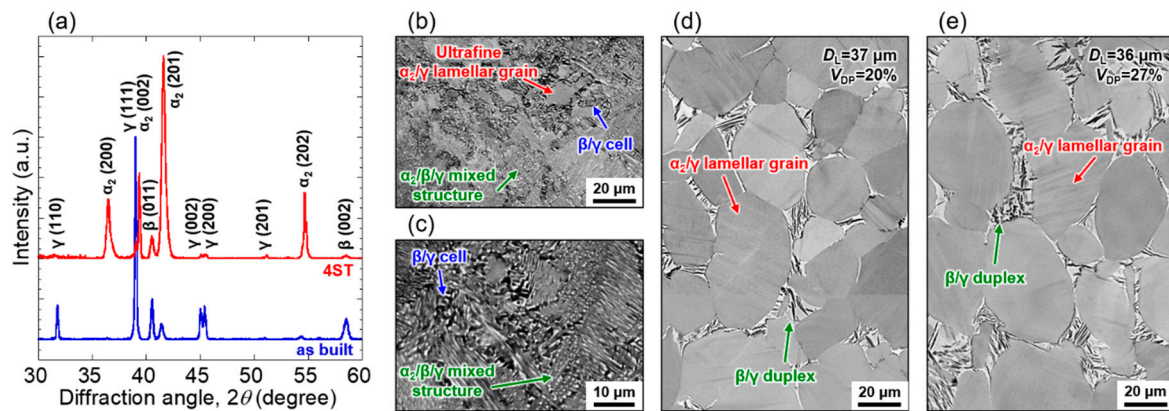


**Figure 2.** Typical XRD profiles of the as-built and 4ST rods (a) and SEM-BSE images of the as-built (b,c), 2ST (d), and 4ST (e) rods. (b) Enlarged image of the area in the as-built rods containing the  $\alpha_2/\beta/\gamma$  mixed structure and the  $\beta/\gamma$  cell.

Meanwhile, the volume fraction of the  $\beta/\gamma$  duplex structure ( $V_{DP}$ ) increases from approximately 20% to 27% with increasing annealing time from 2 h to 4 h (Figure 2d,e). Since the  $\gamma$  phase is precipitated during air cooling from 1573 K, the  $\beta/\gamma$  duplex structure observed after cooling corresponds to the  $\beta$  single phase at 1573 K. The volume fraction of the  $\beta$  phase at 1573 K, estimated from the equilibrium phase diagram of the 44-4 alloy according to the lever rule, is approximately 26% [38]. This means that the microstructure of 4ST is almost in thermodynamic equilibrium, whereas 2ST exhibits a non-equilibrium microstructure. The  $\beta$ -stabilizing element (Cr for the 44-4 alloy) diffuses from the  $\alpha$  grains to the  $\beta$  phase during the solution treatment when the microstructure approaches equilibrium. Therefore, it is considered that the  $\alpha_2/\gamma$  lamellar grains in 2ST contain more solute Cr atoms than their counterparts in 4ST. While the details will be discussed in depth later, a brief comparison of the two solutionized alloys with different concentrations of Cr in the lamellar grains indicates that 2ST is more suitable for aging to form the  $\beta/\gamma$  cell structure.

In the next heat treatment step, 2ST was subjected to aging treatment at 1273 K to obtain the  $\beta/\gamma$  cell structure. Figure 3 shows the typical XRD profiles and SEM-BSE images of the alloys aged for different aging times. The constituent phases of the aged alloys are the  $\alpha_2$ ,  $\gamma$  and  $\beta$  phases, regardless of the aging time (Figure 3a). SEM-BSE images of the alloys aged for different aging times. A cellular structure composed of the  $\beta$  and  $\gamma$  phases can be seen at the grain boundaries of the lamellae even after 0.1 h (Figure 3b). It should be noted that the  $\beta/\gamma$  cells cover the  $\alpha_2/\gamma$  lamellar grains and grow toward the interior of the lamellar grains with increasing aging time (Figure 3c,d). Finally, the lamellar grains are completely replaced by the cells (Figure 3e). The variation in volume fraction of the  $\beta/\gamma$  cells ( $V_C$ ), the  $\alpha_2/\gamma$  lamellar grains ( $V_L$ ) and the coverage of the  $\alpha_2/\gamma$  lamellar grains by the  $\beta/\gamma$  cells and the  $\beta/\gamma$  duplex ( $\theta$ ) as a function of aging time are shown in Figure 4a–c.  $V_C$  of 4ST aged for 1 h is also shown in Figure 4a for comparison. The  $\beta/\gamma$  cells are formed rapidly with a very short incubation time ( $<0.1$  h), resulting in  $V_C$  of approximately 35% and 50% in 0.5AG and 1AG, respectively (Figure 4a). Before aging at 1273 K, the lamellar grains in 2ST are surrounded by the  $\beta/\gamma$  duplex structure and  $\theta$  is approximately 40%, as shown in Figure 4b. On the other hand,  $\theta$  increases to 100% after aging for 0.5 h. It should be noted that  $\theta$  is saturated earlier than  $V_C$ . This means that the cells continue to grow into the grain interior even after the lamellar grains are fully covered by the cells. At the same time,  $V_L$  decreases with the precipitation and growth of the  $\beta/\gamma$  cells and finally reaches 0% after annealing for 24 h (Figure 4c). It should also be noted that  $V_C$  of the aged 4ST is

lower than that of the aged 2ST (1AG), although they were subjected to the same aging conditions (1273 K and 1 h).

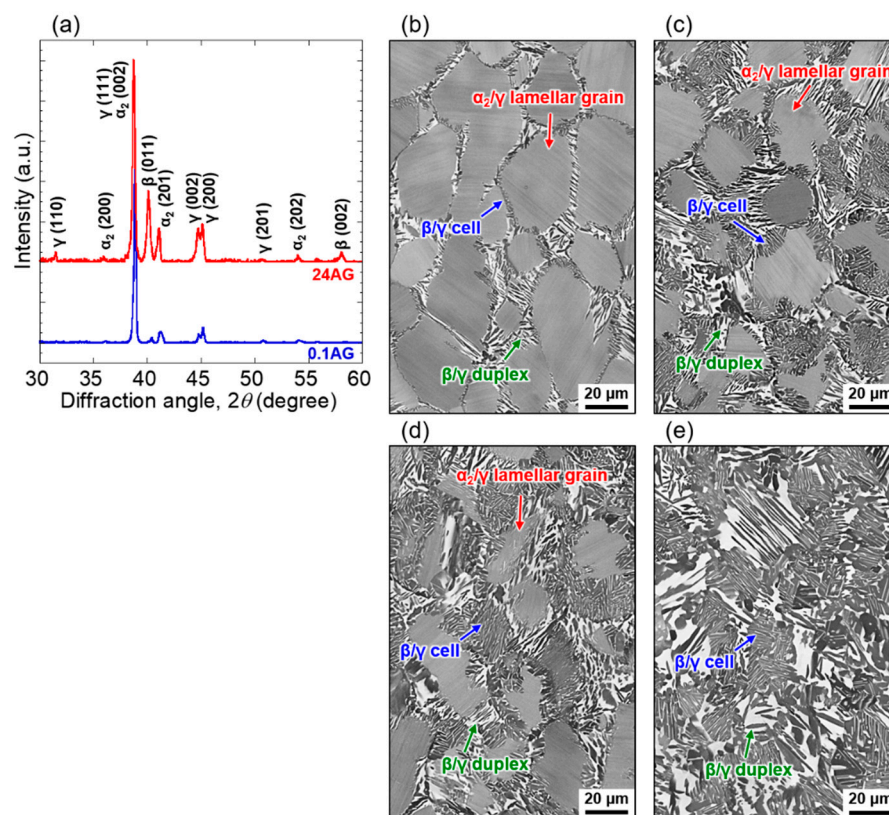


**Figure 3.** Typical XRD profiles of 0.1AG and 24AG (a) and SEM-BSE images of 0.1AG (b), 0.5AG (c), 1AG (d), and 24AG (e).

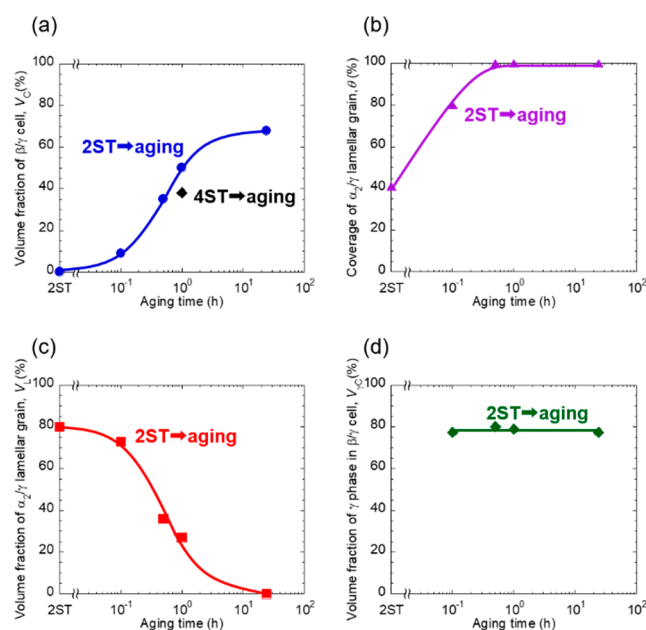


**Figure 4.** Variations in  $V_C$  (a),  $\theta$  (b),  $V_L$  (c), and  $V_{\gamma C}$  (d) as a function of aging time.

Schematic illustrations of microstructural evolution during solution/aging treatments and cellular precipitation at the lamellar grain boundaries are shown in Figure 5. The  $\alpha_2/\gamma$

lamellar structure in which Cr is supersaturated can be obtained by the solution treatment at 1573 K in the  $\beta + \alpha$  two-phase region, followed by air cooling (Figure 5I). When the alloys with the lamellar grains are aged at 1273 K in the  $\beta + \gamma$  two-phase region, the cellular precipitation reaction takes at the lamellar grain boundaries to reduce the Cr concentration in the grains (Figure 5II). The growth rate ( $v$ ) of the cellular structure can be expressed by Equation (2) [46],

$$v = \frac{\lambda D_B (X_0 - X_e^{\alpha\beta})}{l^2 (X_0)} \quad (2)$$

where  $\lambda$  is the thickness of the cell boundary,  $D_B$  represents the cell-boundary diffusivity,  $l$  is the interspace of the cell,  $X_0$  is the concentration of Cr in the untransformed lamellar grain and  $X_e^{\alpha\beta}$  is the concentration of Cr in the  $\gamma$  phase at equilibrium with the  $\beta$  phase. It can be seen that  $v$  depends strongly on  $X_0$ , because  $X_e^{\alpha\beta}$  is determined by the aging temperature. Thus, it can be concluded that the fast precipitation rate of the  $\beta/\gamma$  cells during second step annealing for 2ST results from higher  $X_0$ , compared with 4ST.

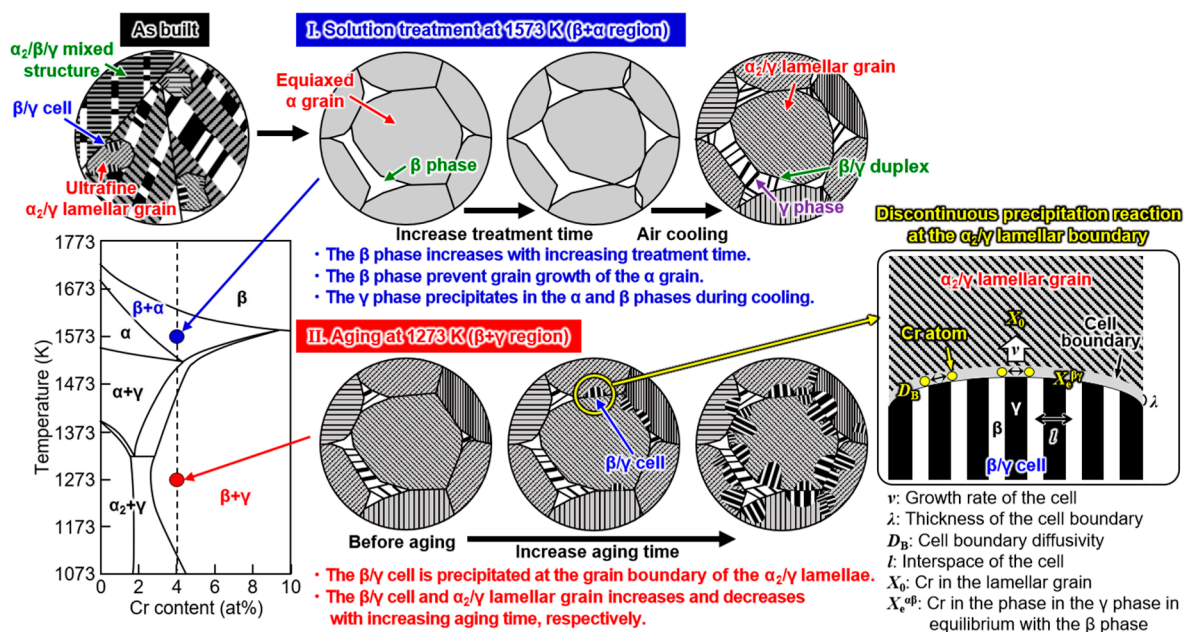


**Figure 5.** Schematic drawing of microstructural evolution during the two-step heat treatment of the 44-4 alloy rods fabricated by EBM.

The variation in the volume fraction of the  $\gamma$  phase in the  $\beta/\gamma$  cells ( $V_{\gamma C}$ ) is plotted against the aging time, as shown in Figure 4d. In the figure, it can be observed that  $V_{\gamma C}$  remains almost constant at approximately 78%, regardless of the aging time. This is because the ratio of the  $\beta$  and  $\gamma$  phases in the cells reflects their equilibrium ratio at the aging temperature. In addition, the morphology of the  $\alpha_2/\gamma$  lamellar structure varies with aging time. Figure 6 shows the bright-field (BF) images and selected area electron diffraction (SAED) patterns of the  $\alpha_2/\gamma$  lamellar grains in the alloys aged at 1273 K for 0.1–1 h. The SAED patterns indicate that the lamellar grains in the alloys are composed of the fine  $\gamma$  plates with twin boundaries and the fine  $\alpha_2$  plates. In addition, the  $\alpha_2$  and  $\gamma$  phases have the Blackburn orientation relationship expressed by Equation (1) (Figure 6d–f). The mean lamellar spacing ( $\lambda$ ) of 0.1AG is approximately 29 nm, which is comparable with that of the ultrafine  $\alpha_2/\gamma$  lamellar grains (approximately 30 nm) in the as-built rods, as reported in a previous study [34]. It is interesting to note that  $\lambda$  increases to approximately 51 nm after aging for 1 h due to coarsening of the  $\gamma$  plates and reduction in the number of the  $\alpha_2$  plates. This is because the aging temperature (1273 K) corresponds to the  $\beta + \gamma$



two-phase region. This minor variation of  $\lambda$  in nano-order size strongly influences the mechanical properties of the alloys.

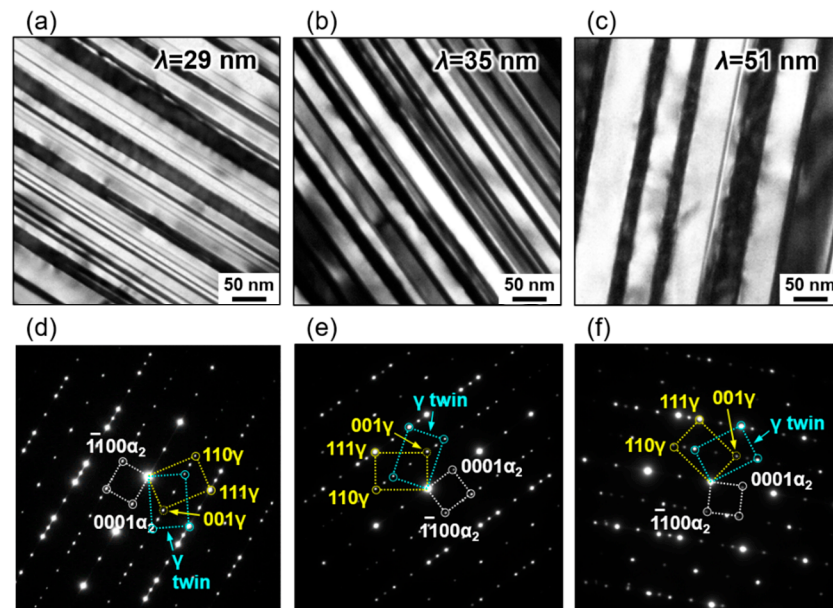


**Figure 6.** Typical BF images (a–c) and SAED patterns (d–f) of the lamellar grains in 0.1AG (a,d), 0.5AG (b,e) and 1AG (c,f) with  $B = [110]_{\gamma} // [1120]_{\alpha_2}$ .

### 3.2. High-Temperature Tensile Properties of the Aged Alloy Rods

The ultimate tensile strength ( $\sigma_B$ ) and the elongation ( $EL$ ) at 1023 K of the as-built rods and the aged rods were examined with respect to the aging time (Figure 7). The  $\sigma_B$  of the as-built alloys is greater than 580 MPa which is higher than that of 48-2-2 alloys fabricated by casting (~450 MPa) [43]. This is because the fine  $\beta$  phase in the  $\alpha_2/\beta/\gamma$  mixed structure and the ultrafine  $\alpha_2/\gamma$  lamellar grains act as strengthening factors at the deformation temperature [34]. It should be noted that the high-temperature strength of the alloys was improved by aging at 1273 K. Moreover, there is no mechanical anisotropy in the aged rods.  $\sigma_B$  of the alloys reaches 697 MPa at 0.1AG and then decreases slightly with increasing aging time. However, it is never less than 600 MPa. As shown in Figure 7b, the as-built rods exhibit  $EL$  of approximately 40% at 1023 K, which is much larger than that of the TiAl alloys produced by other processes (less than 10%) [47]. Such a large ductility at deformation temperatures below 1075 K is one of the unique features of the EB-PBF-TiAl alloys with fine microstructures [33,34]. As described earlier, the microstructures of the aged alloys are relatively coarse and completely different from those of the as-built alloys (Figures 2 and 3). As a result,  $EL$  of 0.1AG decreases steeply to approximately 10%. Figure 7c shows stress–strain ( $S$ – $S$ ) curves of 0.1AG tensile-deformed at 1023 K. The 0.1AG fractures shortly after reaching the maximum stress. Moreover, in the fracture surface of 0.1AG, facets approximately 35  $\mu\text{m}$  in size can be seen with fine steps (Figure 8a). Note that the size of facets is similar to that of  $\alpha_2/\gamma$  lamellar grains. This distinctive fracture surface suggests that brittle crack initiation at the lamellar interface and crack propagation through the lamellar boundary are responsible for the low ductility of 0.1AG. However, it should also be noted that the ductility of the aged alloys can be recovered by increasing aging time, resulting in a high  $EL$  of approximately 36% for 0.5AG and 1AG. In contrast to  $EL$  of 0.1AG, that of 0.5AG increases even beyond UTS (Figure 7c). In addition, the fracture surfaces of 0.5AG pulled to fracture at 1023 K are covered by dimples, indicating that the fracture mode changes to ductile fracture (Figure 8b). Figure 8c shows the side-view of the fractured part of the 0.5AG tensile-deformed alloy specimens. It can be noted that the  $\beta/\gamma$  cells deformed significantly, compared with the  $\alpha_2/\gamma$  lamellar grains. This means

that the cells deformed preferentially during the tensile loading. Furthermore, the crack propagation in the lamellar grains stops at the  $\beta/\gamma$  cells, indicating that the cells act as a barrier to the crack propagation.

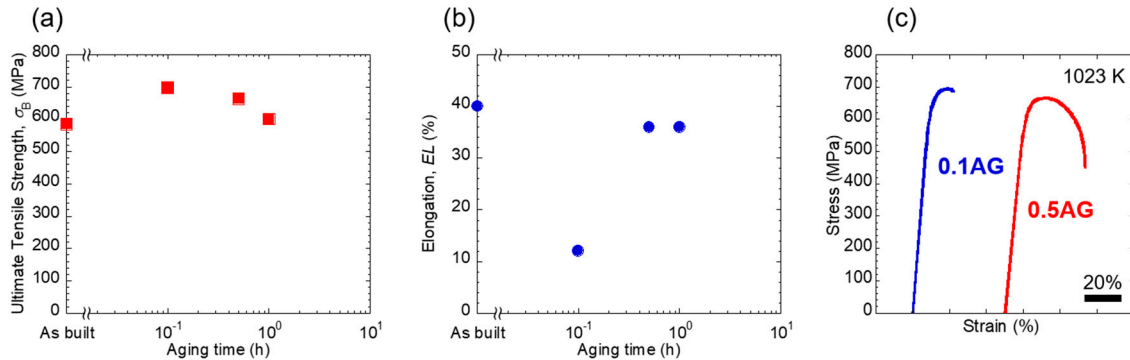


**Figure 7.** Variations in  $\sigma_B$  (a) and EL (b) of the aged alloys at 1023 K with aging time and S–S curves of 0.1AG and 0.5AG tensile deformed at 1023 K (c).

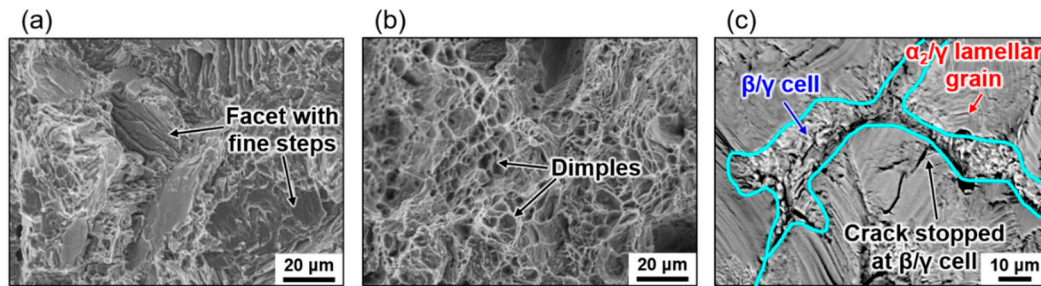


**Figure 8.** Typical SEM fractographs (a,b) and side view SEM image (c) of 0.1AG (a) and 0.5AG (b,c) after tensile deformation to fracture at 1023 K.

These results imply that the high-temperature strength-ductility balance of the 44-4 alloy rods built by EB-PBF can be improved by optimizing their microstructure, focusing on the morphology of the  $\alpha_2/\gamma$  lamellar and the  $\beta/\gamma$  cell structures through the two-step heat treatment proposed in this study. In the rest of this section, we shall discuss the effect of these structures on the tensile properties of heat-treated 44-4 alloys.

### 3.3. Relationship between the Microstructure and High-Temperature Tensile Properties

In order to understand the role of the  $\alpha_2/\gamma$  lamellar grains and the  $\beta/\gamma$  cells on the tensile properties of the alloys, the hardness of these structures was measured by nanoindentation tests and the results are summarized in Figure 9a. The hardness of the lamellar grains is found to be much higher than that of the  $\beta/\gamma$  cells. The lamellar structure is composed of the  $\alpha_2$  phase with the D0<sub>19</sub> structure and the  $\gamma$  phase with the L1<sub>0</sub> structure with the Blackburn relationship. The lamellar boundaries act as a barrier to the propagation of deformation through the Hall–Petch law. Moreover, there are six crystallographic variants in the  $\gamma$  phase. Therefore, not only the  $\alpha_2/\gamma$  boundaries but the  $\gamma/\gamma$  boundaries can be a strong barrier to the deformation propagation across the boundaries [48]. In addition, the degradation of the  $\alpha_2/\gamma$  lamellar grains such as a coarsening of the lamellar spacing cannot be observed in the tensile-deformed specimens, because the lamellar structure has high stability at 1023 K [34]. Therefore, it can be suggested that the  $\alpha_2/\gamma$  lamellar grains play a key role in strengthening the alloys. In fact,  $\sigma_B$  of the aged rods increases with increasing  $V_L$  (Figure 10a). However, the strength of 1AG is lower than the value expected from a linear relationship between  $V_L$  and  $\sigma_B$ , drawn by a dotted line in Figure 10a. This discrepancy is considered to be attributed to the Hall–Petch relationship between the lamellar spacing and the strength [40,41]. Figure 9b shows the Hall–Petch plot for the

nanoindentation hardness of the  $\alpha_2/\gamma$  lamellar grains in the aged alloys. The hardness increases with increasing reciprocal square root of  $\lambda$ . In 1AG, the hardness of the lamellar grains exhibits a low value and approaches that of  $\beta/\gamma$  cells due to high  $\lambda$ , resulting in a low  $\sigma_B$ .

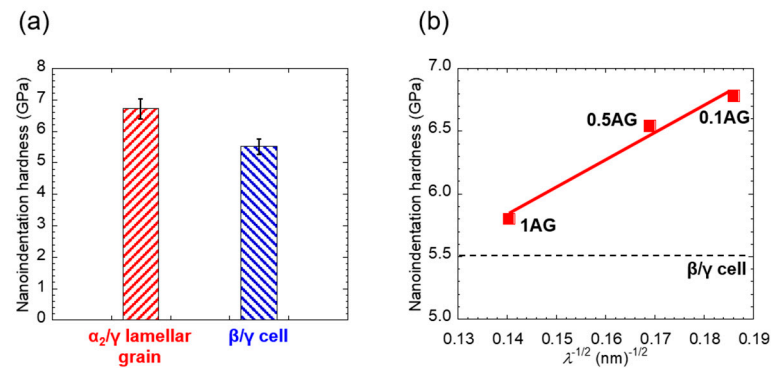


**Figure 9.** Nanoindentation hardness of the  $\alpha_2/\gamma$  lamellar grain and the  $\beta/\gamma$  cell in 0.1AG (a) and Hall–Petch plot of nanoindentation hardness of the  $\alpha_2/\gamma$  lamellar grains in the aged alloys as a function of reciprocal square root of  $\lambda$  (b).

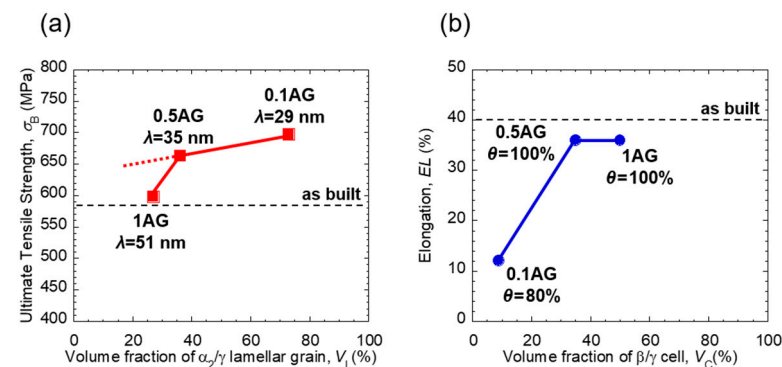


**Figure 10.** Variations in  $\sigma_B$  (a) and EL (b) of the aged rods at 1023 K as a function of  $V_L$  and  $V_C$ , respectively.

In contrast, the ductility of the aged alloys deformed at 1023 K is affected strongly by the presence of the  $\beta/\gamma$  cells at the grain boundaries of the  $\alpha_2/\gamma$  lamellar grains. Although the  $\beta$  phase with ordered B2 structure is a hard phase, the  $\gamma$  phase in the  $\beta/\gamma$  cells is a deformable phase, especially at high temperatures [34]. It is also noted that  $V_{\gamma C}$  is approximately 78%. Thus, the  $\beta/\gamma$  cell can be regarded as a soft region. It should be noted that the hardness of the cell is independent of aging time since  $V_{\gamma C}$  is almost constant in the aged alloys (Figure 4d). Consequently, the crack initiation at the lamellar interface is partially inhibited by the preferential deformation of the  $\beta/\gamma$  cells covering the lamellar grain boundaries (Figure 8c). Furthermore, a few cracks initiated at the lamellar interface are difficult to pass through the lamellar boundaries due to the presence of the ductile cells. Figure 10b shows the relationship between EL and  $V_C$  in the aged alloy rods. It should be noted that EL increases to approximately 36% by increasing  $V_C$  to 35% and then is saturated. At and above  $V_C = 35\%$ , the boundaries of the lamellar grains are fully covered by the  $\beta/\gamma$  cells ( $\theta = 100\%$ ) (Figures 3c and 4b). Therefore,  $\theta$  is also an important factor controlling EL. In other words, EL is not likely to increase further even if  $V_C$  is larger than 35%.

#### 4. Conclusions

The microstructure and high-temperature tensile properties of the  $\beta$ -containing TiAl alloy rods fabricated by EB-PBF and subjected to two-step heat treatment were examined

with a particular focus on the morphology of the  $\alpha_2/\gamma$  lamellar grains and the cellular precipitation reaction at lamellar grain boundaries. The major conclusions of this study were as follows.

1. The 44-4 alloy rods subjected to the solution treatment at 1573 K for 2 h exhibit a non-equilibrium microstructure composed of the  $\alpha_2/\gamma$  lamellar grains with a very fine lamellar spacing and the  $\beta/\gamma$  duplex structure.
2. The  $\beta/\gamma$  cells are formed at the lamellar grain boundaries during aging at 1273 K via the cellular precipitation reaction which is driven by the supersaturation of Cr in the lamellar grains.
3. The  $\beta/\gamma$  cells and the  $\alpha_2/\gamma$  lamellar grains increase and decrease, respectively, with increasing aging time. The fast precipitation rate of the  $\beta/\gamma$  cells in the aged alloys is attributed to the high degree of supersaturation of Cr in the  $\alpha_2/\gamma$  lamellae of the alloys subjected to solution treatment for 2 h.
4.  $\sigma_B$  of the aged alloys containing the  $\alpha_2/\gamma$  lamellar and  $\beta/\gamma$  cell structures exceeds 600 MPa and reaches 697 MPa after 0.1 h of aging. In contrast,  $EL$  of the alloys aged for 0.1 h at 1023 K is approximately 10% which is smaller than that of the as-built alloys. However, the high-temperature ductility of the aged alloys is as high as approximately 36% when they are aged for at least 0.5 h.
5. The volume fraction and the lamellar spacing of the  $\alpha_2/\gamma$  lamellar grains are found to be key factors for improving the high-temperature tensile strength of the aged TiAl alloys. However, the ductility of these alloys is dependent on the morphology of the  $\beta/\gamma$  cells covering the lamellar grain boundaries.

**Author Contributions:** Conceptualization: K.C., H.Y.Y., and M.T.; Investigation: K.C., H.O., K.O., and H.N.; Project administration: H.Y.Y., M.T., and T.N.; Validation: K.C. and H.Y.Y.; Visualization: K.C. and H.O.; Writing—original draft: K.C.; Writing—review and editing: H.Y.Y., H.N., M.T., and T.N. All authors have read and agreed to the published version of the manuscript.

**Funding:** This study was supported by the Council for Science, Technology and Innovation (CSTI), Cross-ministerial Strategic Innovation Promotion Program (SIP), “Materials integration for revolutionary design system of structural materials”, Japan.

**Institutional Review Board Statement:** Not applicable.

**Informed Consent Statement:** Not applicable.

**Data Availability Statement:** The data that support the findings of this study are available from the corresponding author upon reasonable request.

**Conflicts of Interest:** The authors declare that they have no known competing financial interests or personal relationships that could have appeared to influence the work reported in this paper.

## References

1. Kim, Y.W. Ordered intermetallic alloys, part III: Gamma titanium aluminides. *JOM* **1994**, *46*, 30–39. [\[CrossRef\]](#)
2. Bartolotta, P.; Barrett, J.; Kelly, T.; Smashey, R. The use of cast Ti–48Al–2Cr–2Nb in jet engines. *JOM* **1997**, *49*, 48–50. [\[CrossRef\]](#)
3. Aguilar, J.; Schievenbusch, A.; Kätzlitz, O. Investment casting technology for production of TiAl low pressure turbine blades—Process engineering and parameter analysis. *Intermetallics* **2011**, *19*, 757–761. [\[CrossRef\]](#)
4. Bewlay, B.P.; Nag, S.; Suzuki, A.; Weimer, M.J. TiAl alloys in commercial aircraft engines. *Mater. High Temp.* **2016**, *33*, 549–559. [\[CrossRef\]](#)
5. Takeyama, M.; Kobayashi, S. Physical metallurgy for wrought gamma titanium aluminides: Microstructure control through phase transformations. *Intermetallics* **2005**, *3*, 993–999. [\[CrossRef\]](#)
6. Tetsui, T.; Shindo, K.; Kobayashi, S.; Takeyama, M. A newly developed hot worked TiAl alloy for blades and structural components. *Scripta Mater.* **2002**, *47*, 399–403. [\[CrossRef\]](#)
7. Clemens, H.; Wallgram, W.; Kremmer, S.; Güther, V.; Otto, A.; Bartels, A. Design of novel  $\beta$ -solidifying TiAl alloys with adjustable  $\beta/\beta_2$ -phase fraction and excellent hot-workability. *Adv. Eng. Mater.* **2008**, *10*, 707–713. [\[CrossRef\]](#)
8. Bernal, D.; Chamorro, X.; Hurtado, I.; Madariaga, I. Evolution of lamellar microstructures in a cast TNM alloy modified with boron through single-step heat treatments. *Intermetallics* **2020**, *124*, 106842. [\[CrossRef\]](#)



9. Kastnerhuber, M.; Rashkova, B.; Clemens, H.; Mayer, S. Enhancement of creep properties and microstructural stability of intermetallic  $\beta$ -solidifying  $\gamma$ -TiAl based alloys. *Intermetallics* **2015**, *63*, 19–26. [\[CrossRef\]](#)
10. Voisin, T.; Monchoux, J.-P.; Hantcherli, M.; Mayer, S.; Clemens, H.; Couret, A. Microstructures and mechanical properties of a multi-phase  $\beta$ -solidifying TiAl alloy densified by spark plasma sintering. *Acta Mater.* **2014**, *73*, 107–115. [\[CrossRef\]](#)
11. Hadi, M.; Shafyei, A.; Meratian, M. A comparative study of microstructure and high temperature mechanical properties of a  $\beta$ -stabilized TiAl alloy modified by lanthanum and erbium. *Mater. Sci. Eng. A* **2015**, *624*, 1–8. [\[CrossRef\]](#)
12. Jovanović, M.T.; Dimčić, B.; Bobić, I.; Zec, A.; Maksimović, V. Microstructure and mechanical properties of precision cast TiAl turbocharger wheel. *J. Mater. Process. Technol.* **2005**, *167*, 14–21. [\[CrossRef\]](#)
13. Yamaguchi, M. High temperature intermetallics—With particular emphasis on TiAl. *Mater. Sci. Technol.* **1992**, *8*, 299–307. [\[CrossRef\]](#)
14. Renjie, C.; Ming, G.; Hu, Z.; Shengkai, G. Interactions between TiAl alloys and yttria refractory material in casting process. *J. Mater. Process. Technol.* **2010**, *210*, 1190–1196. [\[CrossRef\]](#)
15. Nakano, T.; Fujitani, W.; Ishimoto, T.; Lee, J.W.; Ikeo, N.; Fukuda, H.; Kuramoto, K. Formation of new bone with preferentially oriented biological apatite crystals using a novel cylindrical implant containing anisotropic open pores fabricated by the electron beam melting (EBM) method. *ISIJ Int.* **2011**, *51*, 262–268. [\[CrossRef\]](#)
16. Ikeo, N.; Ishimoto, T.; Nakano, T. Novel powder/solid composites possessing low Young's modulus and tunable energy absorption capacity, fabricated by electron beam melting, for biomedical applications. *J. Alloys Compd.* **2015**, *639*, 336–340. [\[CrossRef\]](#)
17. Harun, W.S.W.; Kamariah, M.S.I.N.; Muhamad, N.; Ghani, S.A.C.; Ahmad, F.; Mohamed, Z. A review of powder additive manufacturing processes for metallic biomaterials. *Powder Technol.* **2018**, *327*, 128–151. [\[CrossRef\]](#)
18. Ishimoto, T.; Ozasa, R.; Nakano, K.; Weinmann, M.; Schnitter, C.; Stenzel, M.; Matsugaki, A.; Nagase, T.; Matsuzaka, T.; Todai, M. Development of TiNbTaZrMo bio-high entropy alloy (BioHEA) super-solid solution by selective laser melting, and its improved mechanical property and biocompatibility. *Scr. Mater.* **2021**, *194*, 113658. [\[CrossRef\]](#)
19. Wang, P.; Huang, P.; Ng, F.L.; Sin, A.J.; Lu, S.; Nai, M.L.S.; Dong, Z.L.; Wei, L. Additively manufactured CoCrFeNiMn high-entropy alloy via pre-alloyed powder. *Mater. Des.* **2019**, *168*, 107576. [\[CrossRef\]](#)
20. Zhai, W.; Wang, P.; Ng, F.L.; Zhou, W.; Nai, S.L.M.; Wei, J. Hybrid manufacturing of  $\gamma$ -TiAl and Ti-6Al-4V bimetal component with enhanced strength using electron beam melting. *Compos. B. Eng.* **2021**, *207*, 108587. [\[CrossRef\]](#)
21. Wartbichler, R.; Clemens, H.; Mayer, S. Electron beam melting of a  $\beta$ -solidifying intermetallic titanium aluminide alloy. *Adv. Eng. Mater.* **2019**, *21*, 1900800. [\[CrossRef\]](#)
22. Hagihara, K.; Nakano, T.; Suzuki, M.; Ishimoto, T.; Sun, S.H. Successful additive manufacturing of MoSi<sub>2</sub> including crystallographic texture and shape control. *J. Alloy Compd.* **2017**, *696*, 67–72. [\[CrossRef\]](#)
23. Gokcekaya, O.; Hayashi, N.; Ishimoto, T.; Ueda, K.; Narushima, T.; Nakano, T. Crystallographic orientation control of pure chromium via laser powder-bed fusion and improved high temperature oxidation resistance. *Addit. Manuf.* **2020**, *36*, 101624.
24. Ishimoto, T.; Wu, S.; Ito, Y.; Sun, S.H.; Amano, H.; Nakano, T. Crystallographic orientation control of 316L austenitic stainless steel via selective laser melting. *ISIJ Int.* **2020**, *60*, 1758–1764. [\[CrossRef\]](#)
25. Ishimoto, T.; Hagihara, K.; Hisamoto, K.; Nakano, T. Stability of crystallographic texture in laser powder bed fusion: Understanding the competition of crystal growth using a single crystalline seed. *Addit. Manuf.* **2021**, *43*, 102004.
26. Gokcekaya, O.; Ishimoto, T.; Hibino, S.; Yasutomi, J.; Narushima, T.; Nakano, T. Unique crystallographic texture formation in Inconel 718 by laser powder bed fusion and its effect on mechanical anisotropy. *Acta Mater.* **2021**, *212*, 116876. [\[CrossRef\]](#)
27. Kan, W.; Chen, B.; Peng, H.; Liang, Y.; Lin, J. Formation of columnar lamellar colony grain structure in a high Nb-TiAl alloy by electron beam melting. *J. Alloys Compd.* **2019**, *809*, 151673. [\[CrossRef\]](#)
28. Karimia, P.; Sadeghi, E.; Ålgårdha, J.; Andersson, J. EBM-manufactured single tracks of Alloy 718: Influence of energy input and focus offset on geometrical and microstructural characteristics. *Mater. Charact.* **2019**, *148*, 88–99. [\[CrossRef\]](#)
29. Kok, Y.; Tan, X.P.; Wang, P.; Nai, M.L.S.; Loh, N.H.; Liu, E.; Tor, S.B. Anisotropy and heterogeneity of microstructure and mechanical properties in metal additive manufacturing: A critical review. *Mater. Des.* **2018**, *139*, 565–586. [\[CrossRef\]](#)
30. Wang, P.; Todai, M.; Nakano, T. Beta titanium single crystal with bone-like elastic modulus and large crystallographic elastic anisotropy. *J. Alloys Compd.* **2018**, *782*, 1–17. [\[CrossRef\]](#)
31. Nakano, T.; Ishimoto, T. Powder-based Additive Manufacturing for Development of Tailor-made Implants for Orthopedic Applications. *KONA* **2015**, *32*, 75–84. [\[CrossRef\]](#)
32. Lee, S.-H.; Todai, M.; Tane, M.; Hagihara, K.; Nakajima, H.; Nakano, T. Biocompatible Low Young's modulus achieved by strong crystallographic elastic anisotropy in Ti-15Mo-5Zr-3Al alloy single crystal. *J. Mech. Behav. Biomed. Mater.* **2012**, *14*, 48–54. [\[CrossRef\]](#)
33. Todai, M.; Nakano, T.; Liu, T.; Yasuda, H.Y.; Hagihara, K.; Cho, K.; Ueda, M.; Takeyama, M. Effect of building direction on the microstructure and tensile properties of Ti-48Al-2Cr-2Nb alloy additively manufactured by electron beam melting. *Addit. Manuf.* **2017**, *13*, 61–70. [\[CrossRef\]](#)
34. Cho, K.; Kawabata, H.; Hayashi, T.; Yasuda, H.Y.; Nakashima, H.; Takeyama, M.; Nakano, T. Peculiar microstructural evolution and tensile properties of  $\beta$ -containing  $\gamma$ -TiAl alloys fabricated by electron beam melting. *Addit. Manuf.* **2021**, *46*, 102091.

35. Cho, K.; Kobayashi, R.; Oh, J.Y.; Yasuda, H.Y.; Todai, M.; Nakano, T.; Ikeda, A.; Ueda, M.; Takeyama, M. Influence of unique layered microstructure on fatigue properties of Ti-48Al-2Cr-2Nb alloys fabricated by electron beam melting. *Intermetallics* **2018**, *95*, 1–10. [[CrossRef](#)]
36. Cho, K.; Kobayashi, R.; Fukuoka, T.; Oh, J.Y.; Yasuda, H.Y.; Todai, M.; Nakano, T.; Ikeda, A.; Ueda, M.; Takeyama, M. Microstructure and Fatigue Properties of TiAl with Unique Layered Microstructure Fabricated by Electron Beam Melting. *Mater. Sci. Forum.* **2018**, *941*, 1597–1602. [[CrossRef](#)]
37. Sakata, M.; Oh, J.Y.; Cho, K.; Yasuda, H.Y.; Todai, M.; Nakano, T.; Ikeda, A.; Ueda, M.; Takeyama, M. Effects of heat treatment on unique layered microstructure and tensile properties of TiAl fabricated by electron beam melting. *Mater. Sci. Forum.* **2018**, *941*, 1366–1371. [[CrossRef](#)]
38. Shaaban, A.; Wakabayashi, H.; Nakashima, H.; Takeyama, M. Phase equilibria among  $\beta/\alpha/\alpha_2/\gamma$  phases and phase transformations in Ti-Al-Cr system at elevated temperatures. *Process. Manuf.* **2019**, *4*, 1471–1476. [[CrossRef](#)]
39. Seifi, M.; Salem, A.A.; Satko, D.P.; Ackelid, U.; Semiatin, S.L.; Lewandowski, J.J. Effects of HIP on microstructural heterogeneity, defect distribution and mechanical properties of additively manufactured EBM Ti-48Al-2Cr-2Nb. *J. Alloys Compd.* **2017**, *729*, 1118–1135. [[CrossRef](#)]
40. Umakoshi, Y.; Nakano, T. The role of ordered domains and slip mode of  $\alpha_2$  phase in the plastic behaviour of TiAl crystals containing oriented lamellae. *Acta Metall. Mater.* **1993**, *41*, 1155–1161. [[CrossRef](#)]
41. Maruyama, K.; Yamada, N.; Sato, H. Effects of lamellar spacing on mechanical properties of fully lamellar Ti-39.4mol% Al alloy. *Mater. Sci. Eng. A* **2001**, *319–321*, 360–363. [[CrossRef](#)]
42. Signori, L.J.; Nakamura, T.; Okada, Y.; Yamagata, R.; Nakashima, H.; Takeyama, M. Fatigue crack growth behavior of wrought  $\gamma$ -based TiAl alloy containing  $\beta$ -phase. *Intermetallics* **2018**, *100*, 77–87. [[CrossRef](#)]
43. Han, L.; Dong, J.; Zhang, S.; Zhang, C.; Xiao, S.; Chen, Y. Microstructure evolution and tensile properties of conventional cast TiAl based alloy with trace Ni addition. *Mater. Sci. Eng. A* **2018**, *715*, 41–48. [[CrossRef](#)]
44. Schwaighofer, E.; Clemens, H.; Mayer, S.; Lindemann, J.; Klose, J.; Smarsly, A.; Güther, V. Microstructural design and mechanical properties of a cast and heat-treated intermetallic multi-phase  $\gamma$ -TiAl based alloy. *Intermetallics* **2014**, *44*, 128–140. [[CrossRef](#)]
45. Cao, G.; Fu, L.; Lin, J.; Zhang, Y.; Chen, C. The relationships of microstructure and properties of a fully lamellar TiAl alloy. *Intermetallics* **2000**, *8*, 647–653. [[CrossRef](#)]
46. Aaronson, H.I.; Liu, Y.C. On the turnbull and the Cahn theories of the cellular reaction. *Scr. Mater.* **1968**, *2*, 1–8. [[CrossRef](#)]
47. Li, M.; Xiao, S.; Chen, Y.; Xu, L.; Tian, J. The effect of carbon addition on the high-temperature properties of  $\beta$  solidification TiAl alloys. *J. Alloys Compd.* **2019**, *775*, 441–448. [[CrossRef](#)]
48. Nakano, T.; Biermann, H.; Riemer, M.; Mughrabi, H.; Nakai, Y.; Umakoshi, Y. Classification of  $\gamma$ - $\gamma$  and  $\gamma$ - $\alpha_2$  lamellar boundaries on the basis of continuity of strains and slip-twinning planes in fatigued TiAl polysynthetically twinned crystals. *Philos. Mag. A* **2001**, *81*, 1447–1471. [[CrossRef](#)]